Horizontal principal stress orientation in the Costa Rica Seismogenesis Project (CRISP) transect from borehole breakouts

Malinverno, A.

Lamont-Doherty Earth Observatory of Columbia University, Palisades, New York, USA

Saito, S.

Institute for Research on Earth Evolution, Japan Agency for Marine-Earth Science and Technology, Yokosuka, Japan

Vannucchi, P.

Dept. of Earth Sciences, Royal Holloway, University of London, Egham, Surrey, UK

Key points:

- Maximum horizontal principal stress (S_{Hmax}) orientations were observed in three drill sites
- S_{Hmax} at the base of a mid-slope site is oriented in the plate convergence direction
- S_{Hmax} directions elsewhere in the sediment cover are variable and likely controlled by normal faulting

Submitted to *Geochemistry, Geophysics, Geosystems* theme "Subduction processes in Central America with an emphasis on CRISP results"

Abstract

The Costa Rica Seismogenesis Project (CRISP) drilled the Pacific margin of the Middle America Trench just north of where the Cocos Ridge enters the subduction zone, resulting in basal erosion of the upper plate. Here we report the orientations of the maximum horizontal principal stress (S_{Hmax}) from borehole breakouts detected by logging-while-drilling and wireline downhole measurements. All S_{Hmax} directions were estimated in the sediment cover of the margin, above the deeper rocks of the deformed margin wedge. We observe three overall S_{Hmax} orientations: NNE-SSW (25° azimuth) in the deepest interval drilled at the upper slope Site U1379; ENE-WSW (82°) in the rest of Site U1379 and in Site U1413, also drilled in the upper slope; and NNW-SSE (157°) in the mid-slope Site U1378. Our preferred interpretation is that the deepest interval of Site U1379 records the stress conditions in the underlying margin wedge, as S_{Hmax} is parallel to the direction of the Cocos-Caribbean plate convergence and of the compressional axes of plate boundary fault earthquakes. The variable S_{Hmax} directions observed elsewhere are likely due to the effect of a network of normal faults that subdivide the sediment cover into a number of independently deforming blocks. In addition, the observed S_{Hmax} directions may be influenced by the subducting Cocos Ridge, which acts as an indenter causing oblique deformation, and by the transition to seismogenic subduction along the plate boundary fault.

Introduction

Subduction at convergent plate margins is a key process in global plate tectonics. Part of the subducted lithosphere is recycled into the mantle, while magmas generated by partial melting result in intense volcanic activity and create new continental crust. Subduction at convergent margins also produces the most powerful and deepest earthquakes on Earth. There are two end-member types of convergent margins, accretionary and erosive [*von Huene and Scholl*, 1991; *Clift and Vannucchi*, 2004]. Accretionary margins are typically found where plate convergence is slow and the underthrusting plate has a relatively thick sediment cover. At the leading edge of the upper plate, these margins contain a prominent accretionary wedge that grows over time by incorporating some of the sediments from the underthrusting, lower plate. In contrast, at erosive margins the upper plate progressively shrinks as its base loses material to the subduction zone. Erosive margins are generally found where plate convergence is fast and the sediment cover on the underthrusting plate is thin [*Clift and Vannucchi*, 2004].

The results presented here were obtained during Integrated Ocean Drilling Program Expeditions 334 and 344 of the Costa Rica Seismogenesis Project [*Vannucchi et al.*, 2012; *Harris et al.*, 2013]. The CRISP transect is located at southern end of the Middle America Trench where the Cocos plate is being subducted beneath the Caribbean plate just north of the Cocos Ridge axis (Figure 1). This location was chosen as an erosive type margin because the subduction of the Cocos Ridge results in a relatively shallow plate boundary fault that makes the upper end of the seismogenic zone accessible to deep riser drilling. In addition to the coring and logging results obtained during the initial phase of CRISP, a 3D seismic survey has been recently acquired [*Bangs et al.*, 2015]. The CRISP project complements the Nankai Trough Seismogenic

68 Zone Experiment (NanTroSEIZE), whose ultimate objective is to drill the seismogenic zone in
69 an accretionary convergent margin [*Tobin et al.*, 2014].

70 Here we report the present orientations of the maximum horizontal principal stress
71 inferred from downhole measurements of borehole breakouts in three sites drilled during the
72 CRISP expeditions (Figures 1-3). The state of stress in the overriding plate controls deformation
73 and faulting, is a function of the coupling at the plate boundary, and can change during the
74 earthquake cycle [*Wang and Hu*, 2006; *Wang et al.*, 2010]. A global survey of lithospheric stress
75 orientation shows that the large scale, first-order patterns of horizontal principal stress directions
76 are controlled by compressional forces applied at plate boundaries [*M L Zoback*, 1992]. Results
77 obtained from borehole breakout analyses in holes drilled on the accretionary Nankai margin
78 sites generally show a maximum horizontal stress direction nearly parallel to the plate
79 convergence, with the exception of a site in the forearc basin where the stress state denotes
80 margin-perpendicular extension [*Chang et al.*, 2010; *Lin et al.*, 2010]. Our results complement
81 the global database of present-day maximum horizontal principal stress directions [*Heidbach et*
82 *al.*, 2009] with measurements in the upper plate of an erosive convergent margin.

83

84

85 **Background**

86

87 The CRISP drilling area is located above the subducting northwest flank of the NE-SW
88 trending aseismic Cocos Ridge (Figures 1 and 2), which consists of thickened oceanic crust
89 produced by Galapagos magmatism and has a relief of 2.5 km over the adjacent ocean floor
90 [*Walther*, 2003]. The subduction of the Cocos Ridge produces basal erosion seaward of the Osa

91 peninsula [*Vannucchi et al.*, 2013]. The Cocos Ridge also acts as an indenter, as shown by the
92 fanning pattern of deformation away from the Cocos Ridge axis measured by GPS [*LaFemina et*
93 *al.*, 2009; *Kobayashi et al.*, 2014]. The Osa peninsula lies on top of the subducted Cocos Ridge
94 axis and its geology suggests that the bulk of the overriding plate there is a Cenozoic mélange
95 resulting from the accretion of oceanic seamounts [*Vannucchi et al.*, 2006]. The Osa peninsula
96 consists of a number of small (1-10 km) blocks bounded by subvertical faults that deform
97 independently in response to the subduction of high-relief asperities on top of the underlying
98 Cocos Ridge [*Vannucchi et al.*, 2006; *Gardner et al.*, 2013].

99 The three CRISP drill sites with breakout measurements are in the mid-slope (U1378)
100 and upper slope (U1379 and U1413) of the convergent margin (Figure 2). On the upper slope,
101 Site U1379 is located in locally flat topography whereas Site U1413 is above a bathymetric scar
102 generated by the subduction of a seamount [*Kluesner et al.*, 2013]. At the leading edge of the
103 upper plate in the CRISP area, an approximately 5-km wide frontal prism of deformed sediment
104 is immediately inland of the trench (Figure 3). The stratigraphy of the frontal prism is
105 comparable to the stratigraphy of the incoming plate with a repetition of the sequence and age
106 inversion, implying the presence of a thrust. Therefore, the frontal prism is an accretionary
107 structure formed by sediments transferred from the incoming plate. Moving inboard across the
108 margin, an apron of Recent to Pleistocene sediments up to ~1 km thick covers unconformably
109 sediments of an older, Pliocene, forearc basin [*Vannucchi et al.*, 2012; *Harris et al.*, 2013]. The
110 three CRISP sites discussed here sampled the Recent to Pleistocene sediment cover; the older
111 Pliocene sediments were reached by drilling only in the deepest portion of Site U1379 (below
112 895 meters below seafloor, or mbsf).

Three-dimensional seismic reflection data have been acquired immediately to the NW of CRISP Sites U1378 and U1379, and Site U1413 was drilled in the area of seismic coverage (Figure 2). In the sediment cover, the seismic data shows a pervasive pattern of small-displacement (tens of meters), closely spaced (~ 200 m) normal faults [*Bangs et al.*, 2015]. These normal faults form two sets, striking NNE-SSW and ENE-WSW. An additional set of E-W striking thrust faults, which tend to form along the crest of anticlinal ridges, is also present. Analyses of the cores obtained in CRISP drilling showed a variety of structures with predominant normal faults and strike-slip faults, typically concentrated in discrete horizons, and subordinate high-angle (dipping 70°-80°) reverse faults [*Vannucchi et al.*, 2012; *Harris et al.*, 2013].

The margin wedge beneath the sediment cover is characterized by three fault systems [*Bangs et al.*, 2015]. Landward dipping thrusts are imaged beneath the lower slope, with few of them reaching the seafloor. Most of these thrust faults are associated to anticlines whose strike rotates from NE-SW to NW-SE moving from the trench to the top of the slope. Beneath the shelf break a second NE-SW set of steep, seaward dipping thrust faults extend through all of the upper plate. This second set produced small offset across some of the normal faults that have formed within the overlying slope cover. The inner part of the wedge has a third set of landward dipping faults similar to the first one beneath the slope. The occurrence of a folded layered sequence in the margin wedge suggests that it is composed of deformed sediments rather than igneous rocks [*Bangs et al.*, 2015].

The 2002 Osa Earthquake occurred near the plate boundary fault at a depth of ~6 km and its epicenter has been located near IODP Site U1413 [*Arroyo et al.*, 2014b]. This and other large earthquakes near the Osa Peninsula (magnitude 6.4-7.4) have focal thrust mechanisms with a

compressional axis parallel the Cocos-Caribbean plate convergence (~N30E). An analysis of recent seismicity in the area shows that the updip limit of the seismogenic zone becomes shallower moving from the NW to the SE toward the Osa peninsula [*Arroyo et al.*, 2014a]. In the 3D seismic data, the distribution of seismicity correlates with a shallowing of the boundary between an updip reflective plate boundary to a downdip weak reflection. This change in reflectivity has been interpreted to mark the transition between a fluid-rich and a well-drained subduction thrust [*Bangs et al.*, 2015]. Almost all the seismic events mapped by *Arroyo et al.* [2014a] occur near the plate boundary fault or within the subducting slab, and they do not provide information on the state of stress within the margin wedge.

Horizontal principal stress orientation and borehole breakouts

One of the principal stresses is perpendicular to the free boundary of the Earth surface, and we follow here the common assumption that the principal stress field in the subsurface lies in approximately vertical and horizontal planes [*M L Zoback*, 1992; *Bell*, 1996; *M D Zoback et al.*, 2003]. With this assumption, the three principal stresses are a vertical stress S_V (given by the weight of the overburden) and two horizontal principal stresses, S_{Hmax} and S_{hmin} (Figure 4). Drilling a vertical borehole through a rock mass that is under different horizontal principal stresses induces a circumferential hoop stress along the borehole wall. This hoop stress depends on the difference $S_{Hmax} - S_{hmin}$ and reaches a maximum at the azimuth of the minimum horizontal stress. If the hoop stress exceeds the compressional rock strength, the borehole wall will fail developing characteristic breakouts located on opposite sides of the hole. These borehole

159 breakouts mark the minimum horizontal stress direction and are key indicators of the state of
160 stress in the subsurface [*M D Zoback et al.*, 2003].

161 Wireline logging measurements can indicate the presence and measure the azimuth of
162 borehole breakouts from the orientation of the arms in caliper tools and from borehole imaging.
163 During IODP Exp. 344, a four-arm caliper tool was deployed to measure high-resolution
164 electrical resistivity images of the borehole wall [*Ekstrom et al.*, 1987]. The resistivity
165 measurements are acquired by four pads on orthogonal arms that are pressed against the borehole
166 wall during the recording. Each pad contains 16 button electrodes that measure a high-resolution
167 resistivity image. The tool also records the aperture of each pair of caliper arms and their
168 orientation with respect to magnetic north. Due to cable torque, this kind of caliper tool rotates
169 while it is being pulled uphole. If breakouts are present, a pair of caliper arms will tend to remain
170 within the breakout, stopping tool rotation. The breakout direction can then be determined from
171 the orientation of the pair of caliper arms that measures the larger borehole diameter [*Bell and*
172 *Gough*, 1979; *Plumb and Hickman*, 1985; *Lin et al.*, 2010].

173 IODP Exp. 344 also used a ultrasonic borehole televiewer [*Zemanek et al.*, 1970]. In this
174 tool, a rotating transducer emits ultrasonic pulses that are reflected by the borehole wall and then
175 received by the same transducer. The continuous rotation of the transducer and the upward
176 motion of the tool produce a complete image of the borehole wall. The borehole televiewer
177 measures both the amplitude and travel time of the reflected ultrasonic pulse. The amplitude is
178 mostly affected by the roughness of the borehole wall, with an additional minor contribution due
179 to the contrast in acoustic impedance between the formation and the borehole fluid. In the
180 amplitude images, the rough breakout surfaces show up as persistent vertical stripes of low
181 reflectivity 180° apart. Measured travel times are converted to hole radius and provide detailed

cross sections of the borehole that show the width and depth of breakouts [*Plumb and Hickman*, 1985; *M D Zoback et al.*, 2003].

Azimuthal measurements acquired by logging-while-drilling (LWD) can also display borehole breakouts. Borehole breakouts are clearly seen in full coverage, high-resolution LWD resistivity images [*Chang et al.*, 2010]. LWD resistivity images were not successfully collected during IODP Exp. 334, but the data acquired included azimuthal caliper measurements from ultrasonic travel times and from a gamma-gamma density log. The azimuthal density caliper measurements are based on the differences in density determined by the near and far detectors, which have different sensitivities to the standoff between the tool and the borehole [*Labat et al.*, 2002]. The LWD tools used in IODP Exp. 334 measured borehole radius in sixteen sectors, and further data processing was necessary to obtain reliable estimates of breakout azimuth, as described in the next section. More details on downhole log measurements acquired during IODP Expeditions 334 and 344 are in the IODP Proceedings [*Vannucchi et al.*, 2012; *Harris et al.*, 2013].

Results

Sites U1378 and U1379, IODP Exp. 334 (LWD data)

The LWD data used to measure breakout orientations consist of azimuthal borehole radii measured by the density tool in 16 sectors (i.e., every 22.5°). To obtain detailed breakout orientations with an angular resolution better than that of the borehole radius measurements, we

fitted to the data an ideal borehole shape consisting of the outer edge of a circle and a concentric ellipse (Figure 5). The azimuth of the fitted major axis of the ellipse defines the breakout orientation, whereas the length of the ellipse axes compared to the radius of the circle give the breakout depth and angle (the angular aperture of the inferred breakout). To estimate the uncertainty of the inferred breakout geometry, we applied a Markov chain Monte Carlo method where the parameters describing the borehole geometry (circle radius, ellipse orientation and axis length) were iteratively perturbed following a random walk. The perturbed values were then accepted or rejected depending on how closely they fit the azimuthal borehole radius measurements following the Metropolis algorithm [*Metropolis et al.*, 1953; *Chib and Greenberg*, 1995]. Example applications of the Metropolis algorithm to geophysical inverse problems are given by *Sen and Stoffa* [1995], *Sambridge and Mosegaard* [2002], and *Malinverno and Briggs* [2004]. In practice, this Monte Carlo procedure returns a large sample of borehole geometry parameters that fit the data. The sampled borehole geometry parameters are converted to breakout geometry parameters (breakout azimuth, depth, and angle). The average of the sampled breakout parameters gives best estimates and the sample variance measures their uncertainty given the data.

The breakout parameter uncertainties determined in the Monte Carlo sampling were used to decide which estimates of breakout geometry were reliable. This step was applied to avoid interpreting as breakouts borehole irregularities caused by other factors, such as an oval-shaped borehole due to drill string abrasion [*Plumb and Hickman*, 1985; *Yassir and Zerwer*, 1997]. The breakout geometry estimates were deemed valid if

- The breakout azimuth was well defined (standard deviation < 5°);

- The breakout depth was significant (estimated depth > twice the standard deviation of breakout depth);
- The breakout angle was not too large (estimated angle < 180° minus twice the standard deviation of breakout angle); this requirement avoids detecting breakouts where the hole is elliptical.

The results of this analysis are in Figure 6. Reliable breakout orientations are consistently around ENE-WSW in the interval 200-440 mbsf of Site U1378. In most of the interval drilled at Site U1379 (300-865 mbsf), the breakouts are instead oriented approximately N-S. At the bottom of Site U1379 (865-895 mbsf), the breakout orientations rotate to about ESE-WNW. The change at 865 mbsf does not coincide with the bottom of the Recent to Pleistocene sedimentary apron, which was detected at 895 mbsf. The Pliocene forearc basin sediments below this depth have markedly greater bulk density and resistivity than those in the overlying younger sediment cover [*Vannucchi et al.*, 2012]. The approximately 50 m-thick interval logged in the Pliocene sediments does not display any breakouts, likely because the formation is stronger than the overlying sediments and the hoop stress is insufficient to fracture it. Also, there was no clear evidence of breakouts in the shallower intervals drilled at these sites (above 200 mbsf in Site U1378 and above 300 mbsf in Site U1379).

Site U1413, IODP Exp. 344 (wireline log data)

During IODP Exp. 344, wireline log measurements for breakout detection were successfully acquired in the interval 95-185 mbsf of Site U1413 (Figure 7). The two pairs of

arms on the resistivity imaging tool measured significantly different borehole diameters in the interval 95-148 mbsf (Figure 7a and 7b). In this depth interval, the resistivity images recorded by pads on the caliper arms that measured the greater hole diameter display lower resistivities (darker image colors in Figure 7c). These observations suggest that a pair of caliper arms was stuck in breakouts during recovery, recording low resistivities because of poor pad contact along the rough borehole wall.

This interpretation is confirmed by the ultrasonic borehole televiewer measurements of reflection amplitude and borehole radius (Figure 7d and 7e, respectively). Ultrasonic reflection amplitudes are relatively low (as expected if the borehole wall is rough) and the borehole radius is larger at the azimuth of the caliper arms that measured the greater hole diameter.

The breakout orientation in the interval 95-148 mbsf can be estimated directly from the azimuth of the caliper arms that measured the greater hole diameter, and is approximately N-S. The rest of the logged interval at Site U1413 does not display breakouts. The caliper arms of the resistivity imaging tool and the ultrasonic borehole radius show a circular hole in the interval 148-170 mbsf. As noted at the base of Site U1379, the absence of breakouts in the 148-170 mbsf interval is likely due to a more compacted and stronger formation that did not fracture due to the hoop stress induced by differences between the horizontal principal stresses. Below 170 mbsf, the borehole becomes very irregular and the hole enlargements do not show a consistent orientation.

Breakout azimuth summary

Estimates of breakout azimuths are summarized in Figure 8, and data files with the values plotted in Figures 6-8 are provided in the Supporting Information. In Sites U1378 and U1413, breakout directions are consistent within the entire depth interval where they were observed, but they clearly differ above and below 865 mbsf at Site U1379. There are essentially three sets of breakout azimuths in our data set. The deepest interval with breakouts in Site U1379 (865-895 mbsf) has an average breakout azimuth of 115° with a standard deviation (σ) of 13°. Breakouts measured above 895 mbsf in Site U1379 and in Site U1413 have the same average orientation of 172° (σ = 15° and 4.8°, respectively). Finally, Site U1378 displays an average breakout direction of 67° (σ = 11°), which is almost perpendicular to that observed in the shallower portion of Site U1379 and in Site U1413. These three sets have relatively small standard deviations and are clearly statistically different.

Discussion

The orientations of the maximum horizontal principal stresses S_{Hmax}, which are perpendicular to the breakout azimuths, are plotted in Figure 9. There are three overall S_{Hmax} orientations: NNE-SSW (25° azimuth) in Site U1379 below 865 mbsf; ENE-WSW (82°) in Site U1413 and Site U1379 above 865 mbsf; and NNW-SSE (157°) in Site U1378. To explain the observed variation in stress orientation, consider the two end members described by *Bell* [1996] for the state of stress in sedimentary sequences. If sediments rest directly on and are

295 mechanically coupled to a deeper unit, the principal stress directions in the sediments will record
296 the signature of the underlying rocks and generally will be spatially uniform. In contrast, if there
297 are intermediate zones of geomechanical weakness such as low strength rocks or fault zones, the
298 sediments will be mechanically detached from the deeper units and principal stress directions
299 will typically vary over short distances. Faults that dissect the sediment sequence can cause
300 some of this spatial variability, because one of the principal stresses will rotate to become locally
301 perpendicular to a mechanically weak fault [*Bell*, 1996; *Yassir and Zerwer*, 1997].

302 S_{Hmax} near the base of the sediment cover in Site U1379 (865-895 mbsf) is oriented in the
303 same direction as the Cocos-Caribbean plate convergence (Figure 9) and the compression
304 direction of thrust earthquakes that occur near the plate boundary fault. The stress state in the
305 upper plate of a convergent margin is controlled by the balance between gravitational force,
306 which promotes margin-perpendicular extension, and shear force along the plate boundary fault,
307 which induces compression [*Wang and He*, 1999; *Wang et al.*, 2010]. The S_{Hmax} direction in the
308 865-895 mbsf interval of Site U1379 may therefore correspond to a compressional state of stress
309 in the margin wedge. This interpretation agrees with observations in Nankai Trough Site C0009,
310 where the S_{Hmax} directions are not constant in the entire drilled interval but rotate in the deeper
311 borehole section, where they become nearly parallel to the direction of plate convergence [*Lin et*
312 *al.*, 2010].

313 The change in S_{Hmax} azimuth at 865 mbsf in Site U1379 coincides with a marked increase
314 in deformation features in the cores and with fluid chemistry anomalies [*Vannucchi et al.*, 2012],
315 and it could be related to a fault. A fault zone near the base of the sediment cover would
316 mechanically detach the sediments from the deeper margin wedge, and the principal stress
317 directions could be dominantly controlled by the pattern of normal faults in the sediment cover.

318 Decoupling of the sediment cover from the deep stress field is also supported by the observation
319 that the S_{Hmax} azimuth in U1413 is the same as that above 865 mbsf in U1379, although the stress
320 field beneath U1413 should be affected by the subduction of a seamount [*Kluesner et al.*, 2013].
321 If a network of faults with different orientations dissects the sediment cover in a number of
322 separate blocks, principal stress directions can be different in different blocks and may rotate
323 near faults within a block. In the CRISP area, 3D seismic reflection images show a network of
324 closely spaced normal faults in the sediment cover [*Bangs et al.*, 2015]. Geological mapping of
325 the Osa peninsula detected two orthogonal sets of normal faults striking NW-SE and NE-SW
326 [*Vannucchi et al.*, 2006]. The strikes of these faults are close to the S_{Hmax} directions in Site
327 U1378 (NNW-SSE) and in Sites U1413 and U1379 above 865 mbsf (ENE-WSW).
328 The simplest interpretation of our results is that the deeper interval of the sediment cover
329 in Site U1379 records the compressional state of stress in the underlying margin wedge, whereas
330 the variable stress directions observed elsewhere are controlled by a network of normal faults in
331 the sediment cover.
332 The principal stress directions may also be affected by other factors. The subducting
333 Cocos Ridge has been proposed to act as an indenter, as shown by a margin-parallel component
334 of forearc deformation measured on Costa Rica GPS land stations [*LaFemina et al.*, 2009;
335 *Kobayashi et al.*, 2014]. With the exception of the deepest interval in Site U1379, the S_{Hmax}
336 directions we observe are approximately parallel and perpendicular to the isobaths of the Cocos
337 Ridge flank and to the most westerly azimuths of the GPS velocities in the land area NW of the
338 Osa peninsula (Figure 9). In principle, the subduction of the Cocos Ridge adjacent to the CRISP
339 sites could cause a counterclockwise rotation of the horizontal principal stresses in the upper
340 plate from the direction of plate convergence. On the other hand, S_{Hmax} in the deeper interval of

341 Site U1379, which should record more closely the state of stress at depth, is parallel to the plate
342 convergence vector and does not seem to be affected by the Cocos Ridge indentation.
343 The change in S_{Hmax} direction between Sites U1378 and U1379 also coincides with the
344 transition projected to the SE of the 3D seismic volume between high and low reflectivity on the
345 plate boundary fault, which has been related to the presence of overpressured fluids (see Fig. 12
346 of *Bangs et al.* [2015]). The updip limit of the seismogenic zone is also approximately located
347 between Sites U1378 and U1379 (see Fig. 1 of *Arroyo et al.* [2014a]). A change in the coupling
348 of the plate boundary fault could result in different states of stress in the upper plate. However,
349 there does not seem to be a straightforward relationship with the S_{Hmax} directions we measure in
350 the sediment cover, as they are mostly oblique to the plate convergence and to the compressional
351 direction of subduction earthquakes.
352 Our conclusions are based only on the orientations of the principal horizontal stresses,
353 and are necessarily limited. To characterize fully the subsurface state of stress, the magnitudes of
354 the principal stress are needed besides their direction, and can be estimated from rock
355 deformation data [*Chang et al.*, 2010]. On the basis of the S_{Hmax} orientation and uniaxial
356 compressional strength tests, *Saito et al.* [2013] suggest that the CRISP upper slope sites (U1379
357 and U1413) are in a normal fault regime and the mid-slope site (U1378) is in a strike-slip regime.
358 Further work will use the S_{Hmax} orientations discussed here to characterize more fully the present
359 state of stress in the CRISP transect.
360
361
362

Conclusions

Borehole breakout orientations obtained from wireline and LWD logs collected during CRISP drilling show three overall orientations of the maximum principal horizontal stress S_{Hmax}: NNE-SSW (25° azimuth) in the deepest interval drilled at the upper slope Site U1379 (865-895 mbsf); ENE-WSW (82°) in the rest of Site U1379 and in Site U1413, also drilled in the upper slope; and NNW-SSE (157°) in the mid-slope Site U1378. All these measurements of S_{Hmax} were obtained in the Recent to Pleistocene sediment cover of the CRISP margin, above the deeper rocks of the deformed margin wedge.

Our preferred interpretation of these results is that the deepest interval of Site U1379 records the stress conditions in the underlying margin wedge, as S_{Hmax} is oriented in the same direction of the Cocos-Caribbean plate convergence and of the compressional axes of thrust earthquakes that occur along the plate boundary fault. The approximately orthogonal S_{Hmax} directions observed in the other intervals are likely due to the effect of a network of normal faults that subdivide the sediment cover into a number of independently deforming blocks. Principal stresses are expected to rotate near low-strength faults, resulting in spatially variable S_{Hmax} directions. In addition, the maximum principal horizontal stress directions may be influenced by the indenting Cocos Ridge, which causes a counterclockwise rotation of deformation vectors, and by the transition between aseismic and seismogenic subduction along the plate boundary fault.

Acknowledgments

This research used samples and data provided by the Integrated Ocean Drilling Program (IODP). The efforts of the JOIDES Resolution shipboard and drilling personnel and of the scientific party of IODP Expeditions 334 and 344 are gratefully acknowledged. We also thank two anonymous reviewers for constructive comments that improved the paper. AM was supported by the U.S. Science Support Program (awards T334A34 and T344B34). Files with the data used in this paper (breakout azimuth estimates in Figures 6-8) are provided in the Supporting Information. This is L-DEO contribution number XXXX.

Figure captions

Figure 1. Location of the CRISP sites (dots) on the Costa Rica Pacific margin. The dotted line is the area in the detailed map in Figure 2 and the yellow arrow indicates the Cocos-Caribbean plate relative motion. MAT = Middle America Trench. Contour interval is 1000 m. The plot was generated with the Generic Mapping Tools (GMT) package [*Wessel et al.*, 2013].

Figure 2. Sites drilled in the CRISP transect during IODP Expeditions 334 and 344, indicating the three sites where borehole breakouts were analyzed. The solid line shows the location of the cross-section in Figure 3. The dotted line outlines the coverage of the 3D seismic reflection survey of *Bangs et al.* [2015]. Bathymetry after *Weinrebe and Ranero* [2012], contour interval 200 m. The plot was generated with the Generic Mapping Tools (GMT) package [*Wessel et al.*, 2013].

Figure 3. Schematic cross-section through the CRISP drilling transect. Unit geometry after *Vannucchi et al.* [2012].

Figure 4. Relationship between orientation of borehole breakouts and of minimum and maximum principal horizontal stress directions (S_{hmin} and S_{Hmax}, respectively). Breakouts form if the compressional hoop stress on the borehole wall, which is maximum at the S_{hmin} azimuth, overcomes the rock strength.

419 Figure 5. Breakout geometry parameters (azimuth, depth, and angle) are estimated by fitting an
420 idealized borehole shape (the outer boundary of a concentric circle and ellipse) to LWD
421 measurements of the borehole radius collected in a 2 m-thick interval (black dots).
422
423 Figure 6. Estimated breakout azimuths in 2 m-thick hole intervals (dots) and borehole radius
424 images from LWD density measurements in Sites U1378 and U1379. Uncertainties in borehole
425 azimuth (± two standard deviations) are shown as horizontal lines; in most cases uncertainties are
426 smaller than the size of the plotted dot. The three images on the right span the total interval with
427 breakouts in U1379, and the dashed lines connect points at the same depth.
428
429 Figure 7. Breakout-related wireline log measurements in Site U1413. The borehole diameters
430 measured by the two pairs of caliper arms on the resistivity imaging tool are in (a) and (b). The
431 resistivity image is in (c) and images with the amplitude and hole radius measured by the
432 ultrasonic televiewer tool are in (d) and (e). The azimuth of the caliper arms that show the
433 greater borehole diameter in the interval 95-148 mbsf is also shown in (c), (d), and (e).
434
435 Figure 8. Circular histograms of breakout azimuths measured at Sites U1378, U1379, and
436 U1413. Averages of measured breakout azimuths are plotted as thick dashed lines. Labels show
437 the average and standard deviation (σ) of the breakout azimuths measured in each interval.
438
439 Figure 9. S_{Hmax} orientations (red lines) in three CRISP sites. The blue line segment indicates the
440 S_{Hmax} direction measured below 865 mbsf in Site U1379; the red line segments show the S_{Hmax}
441 direction at depths above 865 mbsf in Site U1379 and in the whole depth interval where

442 breakouts were detected in Sites U1378 and U1413. The yellow arrow denotes the Cocos-
443 Caribbean plate relative motion. The black arrows span the range of GPS velocity directions
444 measured with respect to the Caribbean plate on the Costa Rica mainland NW of the Osa
445 peninsula [*LaFemina et al.*, 2009]. Bathymetry after *Weinrebe and Ranero* [2012], contour
446 interval 200 m. The plot was generated with the Generic Mapping Tools (GMT) package
447 [*Wessel et al.*, 2013].
448
449

References

Arroyo, I. G., S. Husen, and E. R. Flueh (2014a), The seismogenic zone in the Central Costa Rican Pacific margin: high-quality hypocentres from an amphibious network, *Int. J. Earth Sci.*, *103*, 1747-1764, doi:10.1007/s00531-013-0955-8.

Arroyo, I. G., I. Grevemeyer, C. R. Ranero, and R. von Huene (2014b), Interplate seismicity at the CRISP drilling site: The 2002 Mw 6.4 Osa Earthquake at the southeastern end of the Middle America Trench, *Geochem. Geophys. Geosyst.*, *15*, 3035-3050, doi:10.1002/2014GC005359.

Bangs, N. L., K. D. McIntosh, E. A. Silver, J. W. Kluesner, and R. C. R. (2015), Fluid accumulation along the Costa Rica subduction thrust and development of the seismogenic zone: The Costa Rica subduction thrust and development of the seismogenic zone, *J. Geophys. Res.*, *120*, 67-86, doi:10.1002/2014JB011265.

Bell, J. S. (1996), In situ stresses in sedimentary rocks (part 2): Applications of stress measurements, *Geosci. Canada*, *23*, 135-153.

Bell, J. S., and D. I. Gough (1979), Northeast-southwest compressive stress in Alberta: Evidence from oil wells, *Earth Planet. Sci. Lett.*, *45*, 475-482.

Chang, C., L. C. McNeill, J. C. Moore, W. Lin, M. Conin, and Y. Yamada (2010), In situ stress state in the Nankai accretionary wedge estimated from borehole wall failures, *Geochem. Geophys. Geosyst.*, *11*, Q0AD04, doi:10.1029/2010GC003261.

Chib, S., and E. Greenberg (1995), Understanding the Metropolis-Hastings algorithm, *The American Statistician*, *49*, 327-335.

Clift, P., and P. Vannucchi (2004), Controls on tectonic accretion versus erosion in subduction zones: Implications for the origin and recycling of the continental crust, *Rev. Geophys.*, *42*, RG2001, doi:10.1029/2003RG000127.

Ekstrom, M. P., C. Dahan, M.-Y. Chen, P. Lloyd, and D. J. Rossi (1987), Formation imaging with microelectrical scanning arrays, *Log Analyst*, *28*, 294-306.

Gardner, T. W., D. M. Fisher, K. D. Morell, and M. L. Cupper (2013), Upper-plate deformation in response to flat slab subduction inboard of the aseismic Cocos Ridge, Osa Peninsula, Costa Rica, *Lithosphere*, *5*, 247-264, doi:10.1130/L251.1.

Harris, R. N., A. Sakaguchi, K. E. Petronotis, and Expedition 344 Scientists (2013), *Proceedings IODP, Exp. 344*, Integrated Ocean Drilling Program Management International, Inc.

Heidbach, O., M. Tingay, A. Barth, J. Reinecker, D. Kurfeß, and B. Müller (2009), *The World Stress Map based on the database release 2008*, Commission for the Geological Map of the World, doi:10.1594/GFZ.WSM.Map2009, Paris.

Kluesner, J. W., E. A. Silver, J. Gibson, N. L. Bangs, K. D. McIntosh, D. Orange, C. R. Ranero, and R. von Huene (2013), High density of structurally controlled, shallow to deep water fluid seep indicators imaged offshore Costa Rica, *Geochem. Geophys. Geosyst.*, *14*, 519-539, doi:10.1002/ggge.20058.

Kobayashi, D., P. LaFemina, H. Geirsson, E. Chichaco, A. A. Abrego, H. Mora, and E. Camacho (2014), Kinematics of the western Caribbean: Collision of the Cocos Ridge and upper plate deformation, *Geochem. Geophys. Geosyst.*, *15*, 1671-1683, doi:10.1002/2014GC005234.

493 Labat, C., S. Brady, M. Everett, D. Ellis, M. Doghmi, J. C. Tomlinson, and G. Shehab (2002),
494 3D azimuthal LWD caliper, *SPE Annual Tech. Conf. Exhib., San Antonio*, *SPE 77526*.
495 LaFemina, P., T. H. Dixon, R. Govers, E. Norabuena, H. Turner, A. Saballos, G. Mattioli, M.
496 Protti, and W. Strauch (2009), Fore-arc motion and Cocos Ridge collision in Central
497 America, *Geochem. Geophys. Geosyst.*, *10*, Q05S14, doi:10.1029/ 2008GC002181.
498 Lin, W., et al. (2010), Present-day principal horizontal stress orientations in the Kumano forearc
499 basin of the southwest Japan subduction zone determined from IODP NanTroSEIZE
500 drilling Site C0009, *Geophys. Res. Lett.*, *37*, L13303, doi:10.1029/2010GL043158.
501 Malinverno, A., and V. A. Briggs (2004), Expanded uncertainty quantification in inverse
502 problems: Hierarchical Bayes and empirical Bayes, *Geophysics*, *69*, 1005-1016,
503 doi:10.1190/1.1778243.
504 Metropolis, N., A. W. Rosenbluth, M. N. Rosenbluth, A. H. Teller, and E. Teller (1953),
505 Equation of state calculations by fast computing machines, *J. Chem. Phys.*, *21*, 1087-
506 1092.
507 Plumb, R. A., and S. H. Hickman (1985), Stress-induced borehole elongation: A comparison
508 between the four-arm dipmeter and the borehole televiewer in the Auburn geothermal
509 well, *J. Geophys. Res.*, *90*, 5513-5521.
510 Saito, S., A. Malinverno, W. Lin, Y. Yamamoto, H. Wu, R. N. Harris, A. Sakaguchi, K. Ujiie, P.
511 Vannucchi, and K. E. Petronotis (2013), Preliminary results on horizontal stress
512 orientation and stress magnitude off Osa Peninsula, Costa Rica, paper presented at 2013
513 Fall Meeting, AGU, Abstract T31G-2595, San Francisco, Calif., 9-13 Dec.
514 Sambridge, M., and K. Mosegaard (2002), Monte Carlo methods in geophysical inverse
515 problems, *Rev. Geophys.*, *40(3)*, 1009, doi:10.1029/2000RG000089.
516 Sen, M. K., and P. L. Stoffa (1995), *Global Optimization Methods in Geophysical Inversion*,
517 Elsevier, Amsterdam.
518 Tobin, H., P. Henry, P. Vannucchi, and E. Screaton (2014), Subduction Zones: Structure and
519 Deformation History, in *Earth and Life Processes Discovered from Subseafloor*
520 *Environment – A Decade of Science Achieved by the Integrated Ocean Drilling Program*
521 *(IODP)*, edited by R. Stein, D. Blackman, F. Inagaki and H.-C. Larsen, pp. 599-640,
522 doi:10.1016/B978-0-444-62617-2.00020-7, Elsevier, Amsterdam/New York.
523 Vannucchi, P., D. M. Fisher, T. W. Gardner, and S. Bier (2006), From seamount accretion to
524 tectonic erosion: Formation of Osa Mélange and the effects of Cocos Ridge subduction in
525 southern Costa Rica, *Tectonics*, *25*, TC2004, doi:10.1029/2005TC001855.
526 Vannucchi, P., K. Ujiie, N. Stroncik, A. Malinverno, and Expedition 334 Scientists (2012),
527 *Proceedings IODP, Exp. 334*, Integrated Ocean Drilling Program Management
528 International, Inc.
529 Vannucchi, P., P. B. Sak, J. Phipps Morgan, K. Ohkushi, K. Ujiie, and IODP Expedition 334
530 Shipboard Scientists (2013), Rapid pulses of uplift, subsidence, and subduction erosion
531 offshore Central America: Implications for building the rock record of convergent
532 margins, *Geology*, *41*, 995-998, doi:10.1130/G34355.1.
533 von Huene, R., and D. W. Scholl (1991), Observations at convergent margins concerning
534 sediment subduction, subduction erosion, and the growth of continental crust, *Rev.*
535 *Geophys.*, *29*, 279-316.
536 Walther, C. H. E. (2003), The crustal structure of the Cocos ridge off Costa Rica, *J. Geophys.*
537 *Res.*, *108*, 2136, doi:10.1029/2001JB000888.

538 Wang, K., and J. He (1999), Mechanics of low-stress forearcs: Nankai and Cascadia, *J. Geophys.*
539 *Res.*, *104*, 15191-15205, doi:10.1029/1999JB900103.
540 Wang, K., and Y. Hu (2006), Accretionary prisms in subduction earthquake cycles: The theory
541 of dynamic Coulomb wedge, *J. Geophys. Res.*, *111*, B06410,
542 doi:10.1029/2005JB004094.
543 Wang, K., Y. Hu, R. von Huene, and N. Kukowski (2010), Interplate earthquakes as a driver of
544 shallow subduction erosion, *Geology*, *38*, 431-434, doi:10.1130/G30597.1.
545 Weinrebe, W., and C. R. Ranero (2012), Multibeam bathymetry compilation of the Central
546 America Pacific Margin, *Integrated Earth Data Applications (IEDA)*,
547 doi:10.1594/IEDA/100069.
548 Wessel, P., W. H. F. Smith, R. Scharroo, J. Luis, and F. Wobbe (2013), Generic Mapping Tools:
549 Improved version released, *EOS, Trans. AGU*, *94*, 409-410.
550 Yassir, N. A., and A. Zerwer (1997), Stress regimes in the Gulf Coast, offshore Louisiana: Data
551 from well-bore breakout analysis, *Am. Ass. Petr. Geol. Bull.*, *81*, 293-307.
552 Zemanek, J., E. E. Glenn, L. J. Norton, and R. L. Caldwell (1970), Formation evaluation by
553 inspection with the borehole televiewer, *Geophysics*, *35*, 254-269.
554 Zoback, M. D., C. A. Barton, M. Brudy, D. A. Castillo, T. Finkbeiner, B. R. Grollimund, D. B.
555 Moos, P. Peska, C. D. Ward, and D. J. Wiprut (2003), Determination of stress orientation
556 and magnitude in deep wells, *Int. J. of Rock Mech. and Mining Sci.*, *40*, 1049-1076,
557 doi:10.1016/j.ijrmms.2003.07.001.
558 Zoback, M. L. (1992), First- and second-order patterns of stress in the lithosphere: The World
559 Stress Map project, *J. Geophys. Res.*, *97*, 11,703-11,728.
560

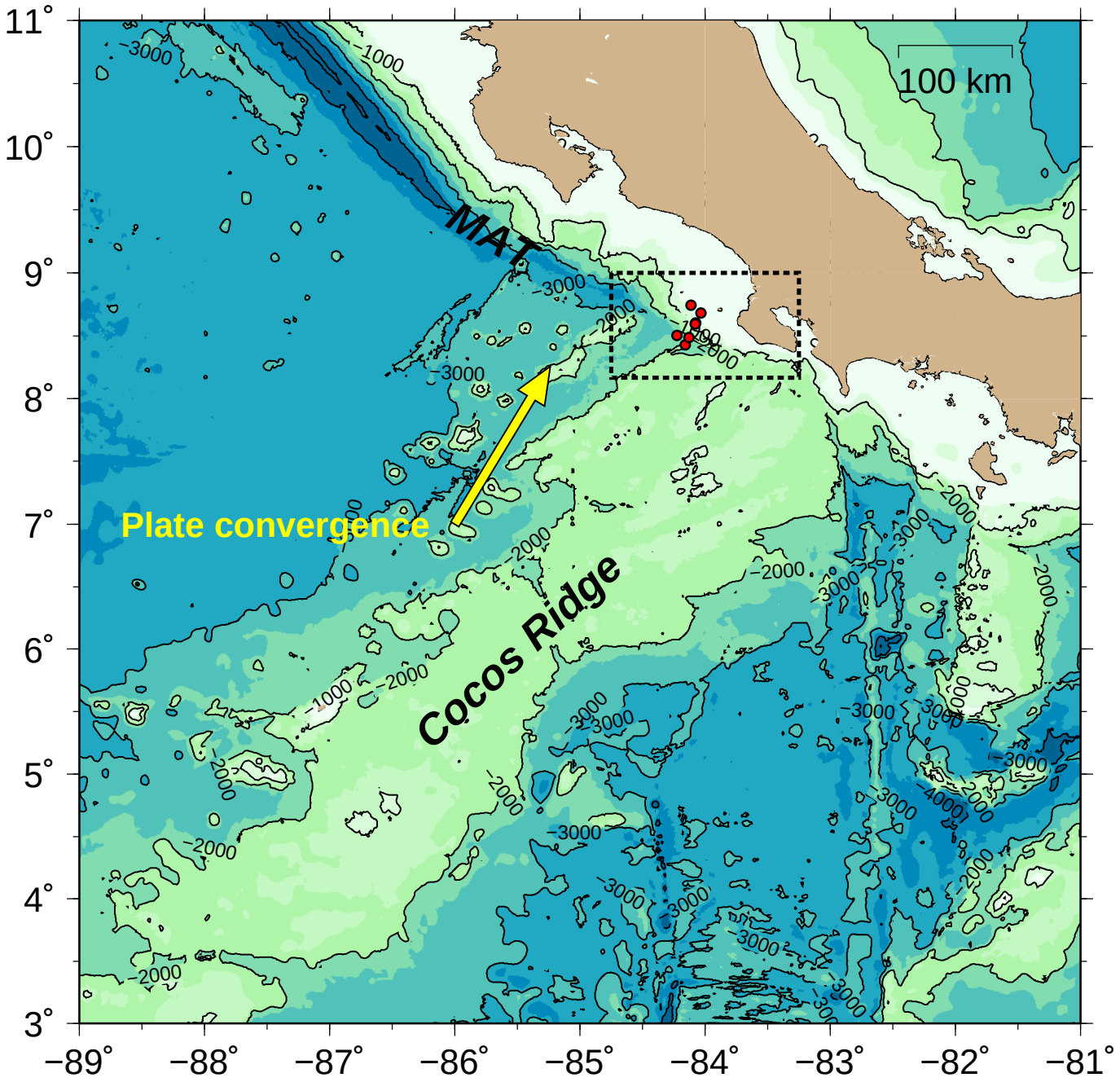
11°
10°
9°
8°
7°
6°
5°
4°
3°
−89°
−88°
−87°
−86°
−85°
−84°
−83°
−82°
−81°
100 km
MAT
Plate convergence
Cocos Ridge
−3000
−1000
−2000
3000
−4000

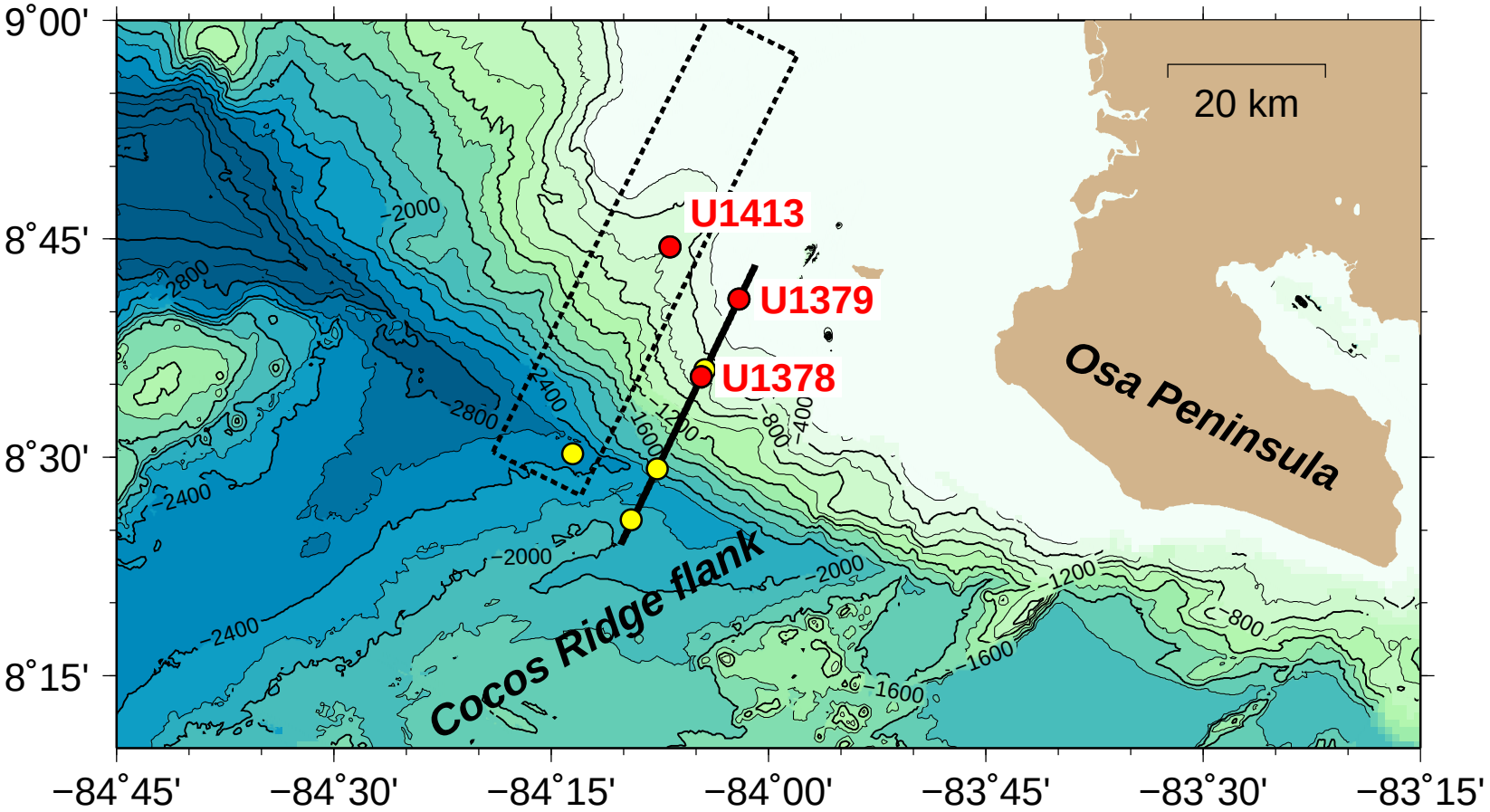
9°00'
8°45'
8°30'
8°15'
−84°45'
−84°30'
−84°15'
−84°00'
−83°45'
−83°30'
−83°15'
20 km
U1413
U1379
U1378
Osa Peninsula
Cocos Ridge flank
−2000
−2800
−2400
−1600
−1200
−800
−400

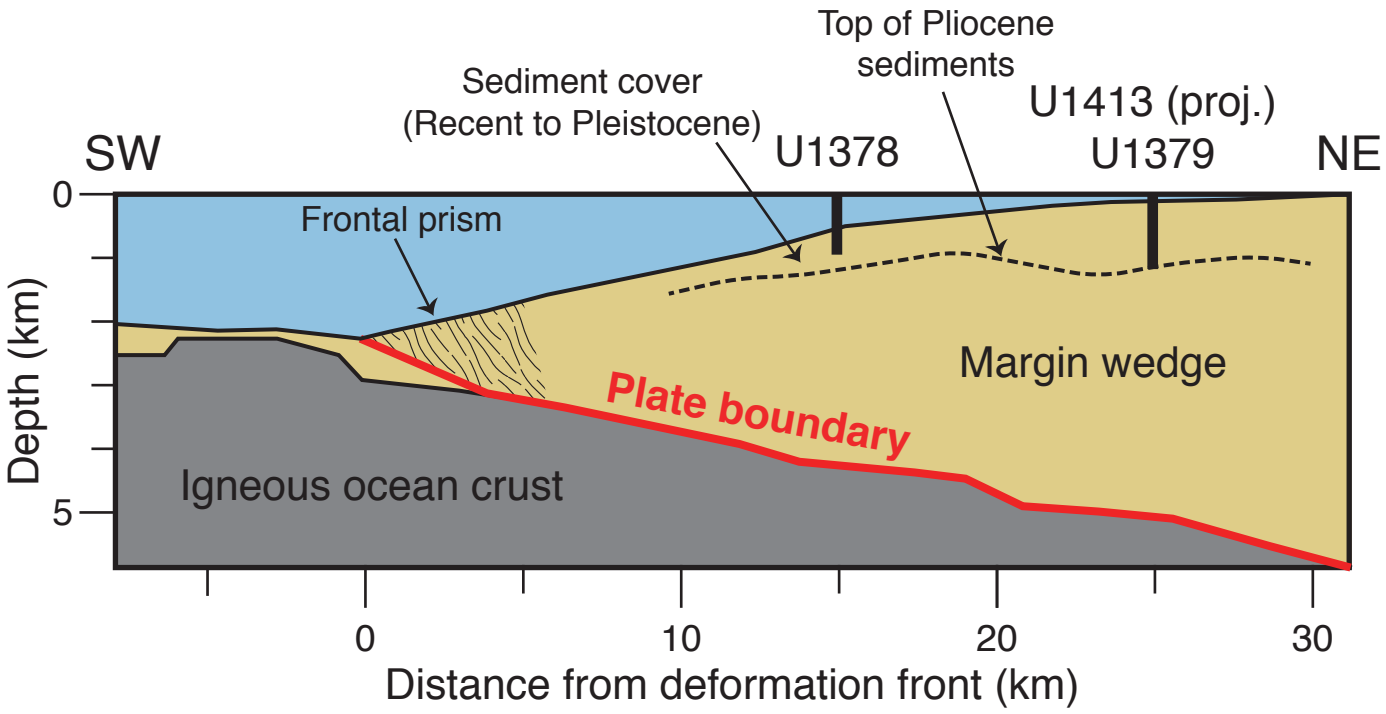
Top of Pliocene
sediments
Sediment cover
(Recent to Pleistocene)
U1413 (proj.)
SW
U1378
U1379
NE
0
Frontal prism
Depth (km)
Margin wedge
Plate boundary
Igneous ocean crust
5
0
10
20
30
Distance from deformation front (km)

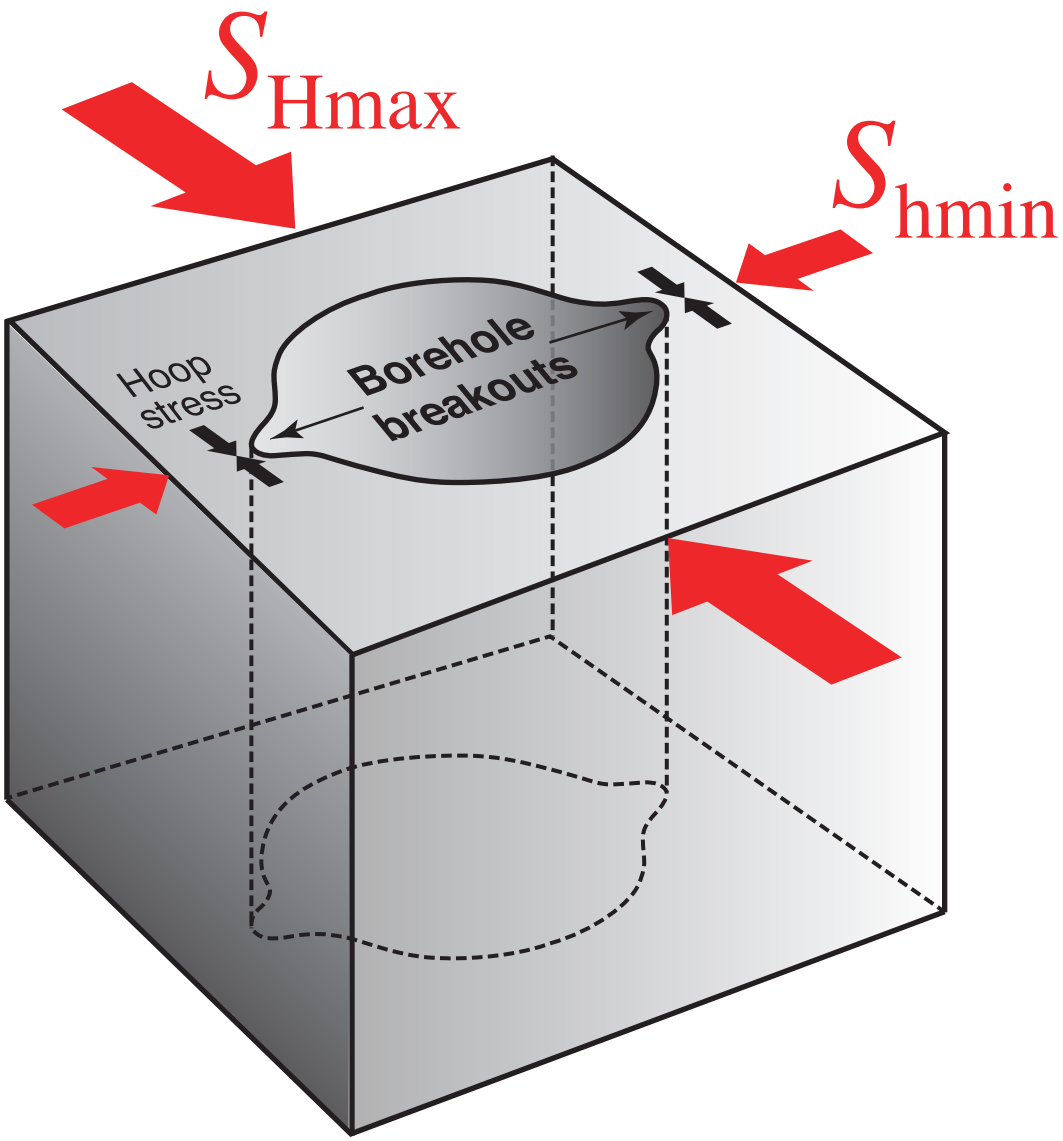
S_{Hmax}
S_{hmin}
Hoop stress
Borehole breakouts

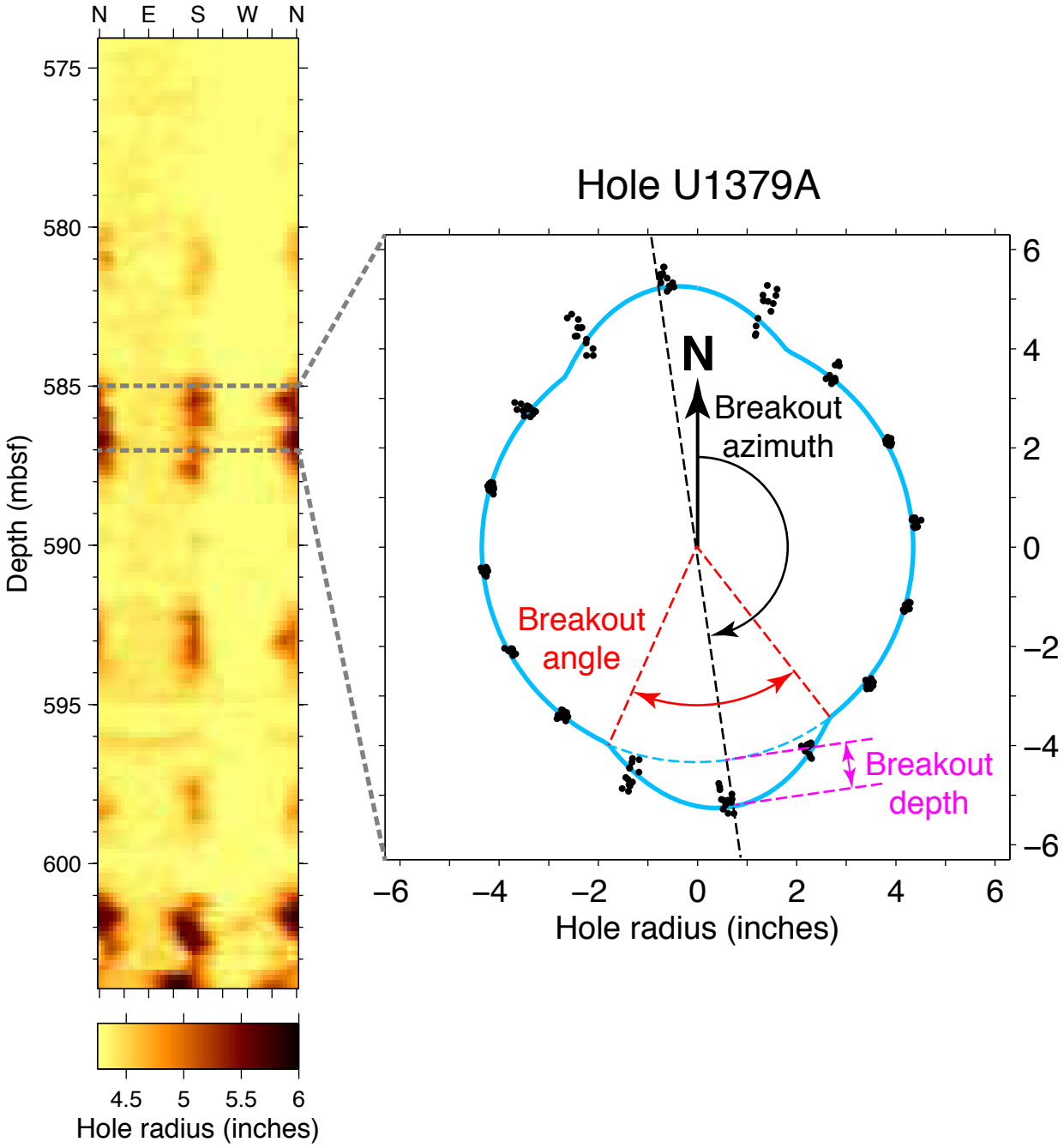
N E S W N
575
580
585
590
595
600
Depth (mbsf)
4.5 5 5.5 6
Hole radius (inches)
Hole U1379A
N
Breakout azimuth
Breakout angle
Breakout depth
6 4 2 0 −2 −4 −6
−6 −4 −2 0 2 4 6
Hole radius (inches)

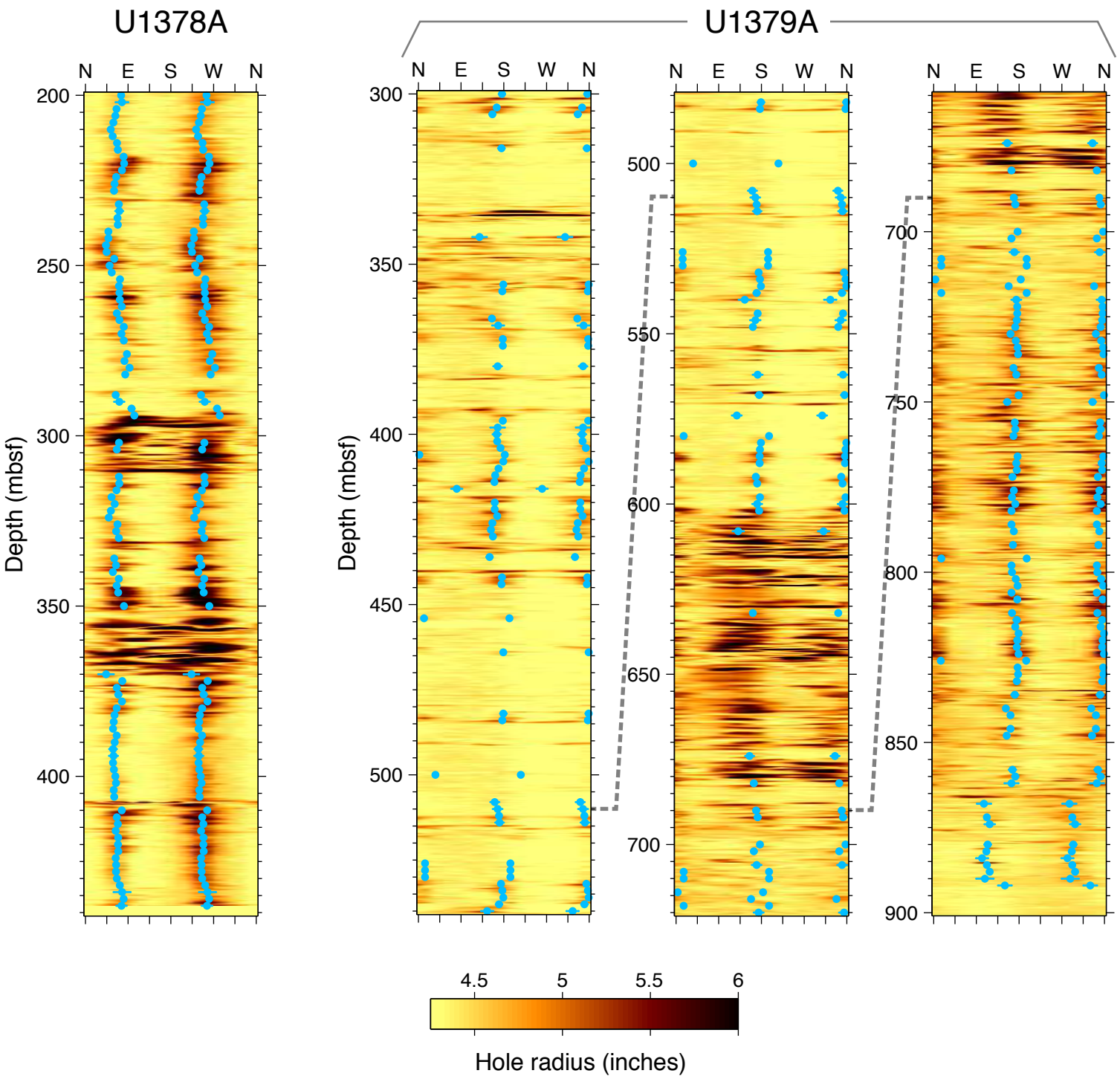
U1378A
U1379A
N E S W N
Depth (mbsf)
200
250
300
350
400
300
350
400
450
500
500
550
600
650
700
700
750
800
850
900
4.5
5
5.5
6
Hole radius (inches)

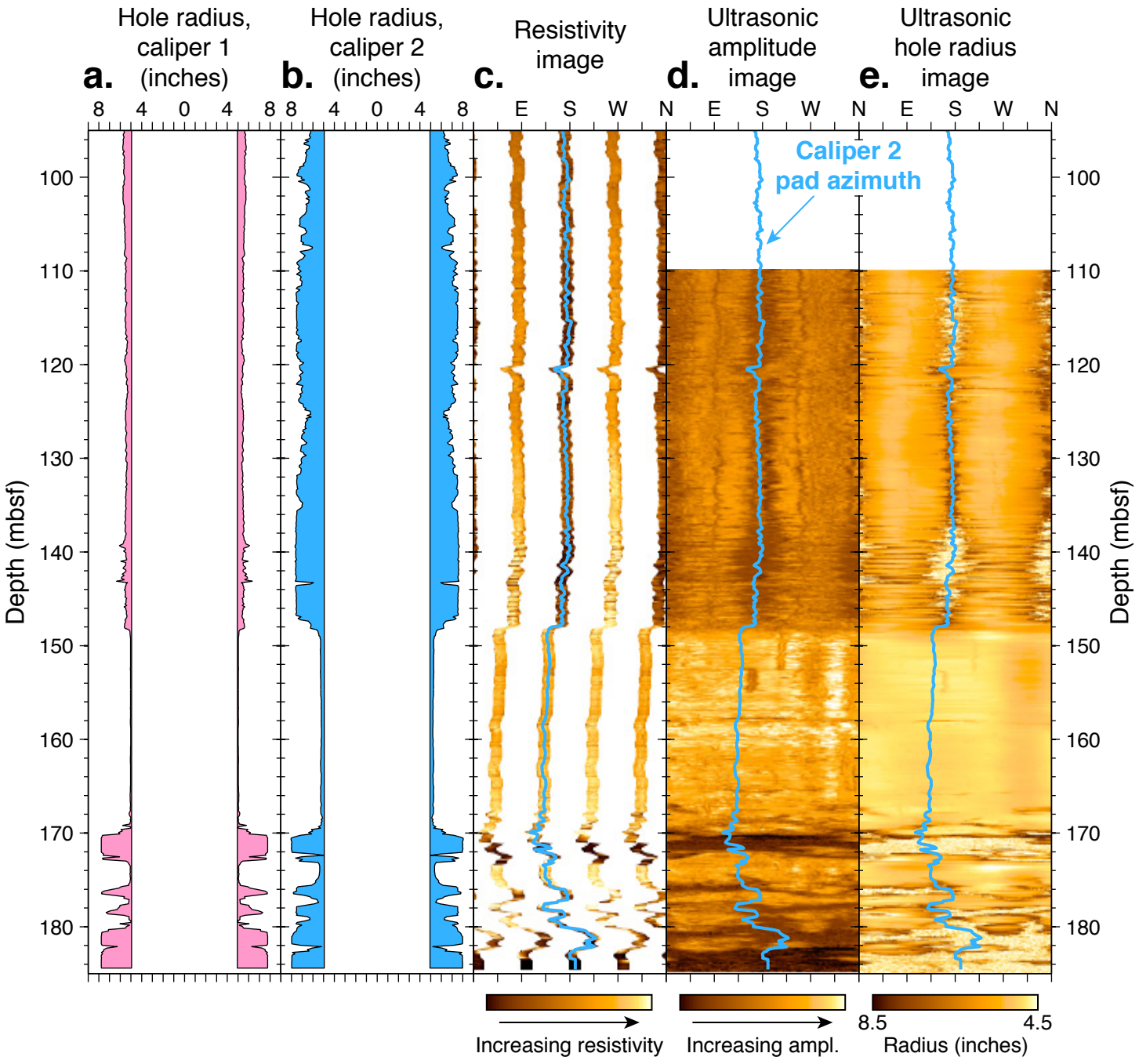
a.
Hole radius, caliper 1 (inches)
b.
Hole radius, caliper 2 (inches)
c.
Resistivity image
d.
Ultrasonic amplitude image
e.
Ultrasonic hole radius image
8 4 0 4 8
E S W N
Caliper 2 pad azimuth
Depth (mbsf)
100
110
120
130
140
150
160
170
180
Increasing resistivity
Increasing ampl.
8.5
4.5
Radius (inches)

U1378A (200–440 mbsf, N=97)

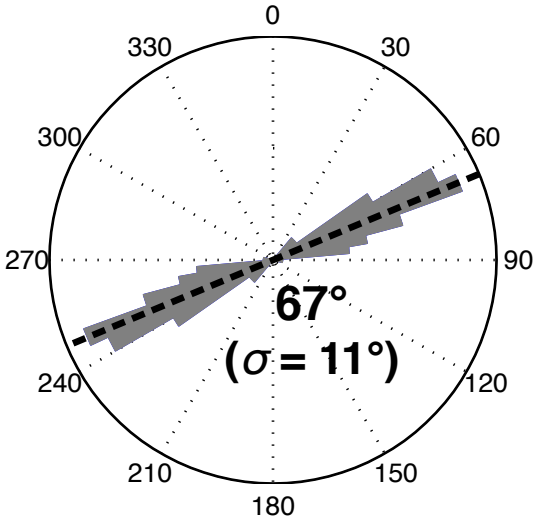

U1413C (95–148 mbsf, N=348)

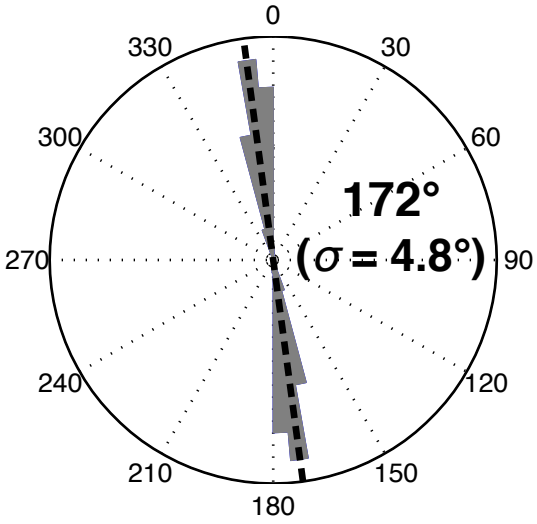

U1379A (865–895 mbsf, N=10)

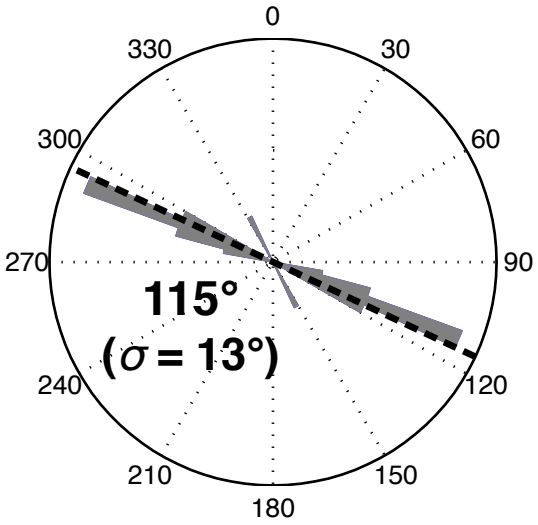

U1379A (300–865 mbsf, N=132)

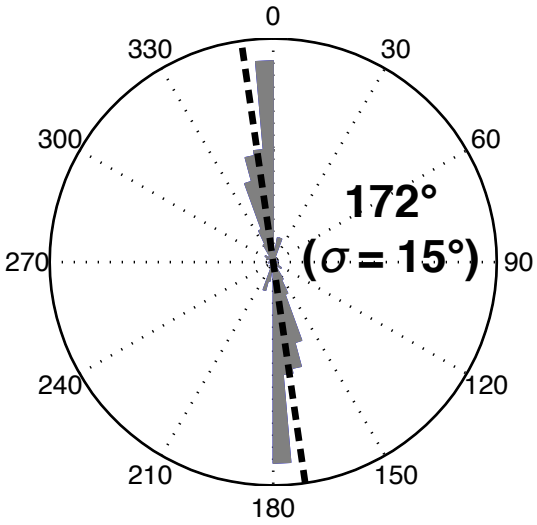

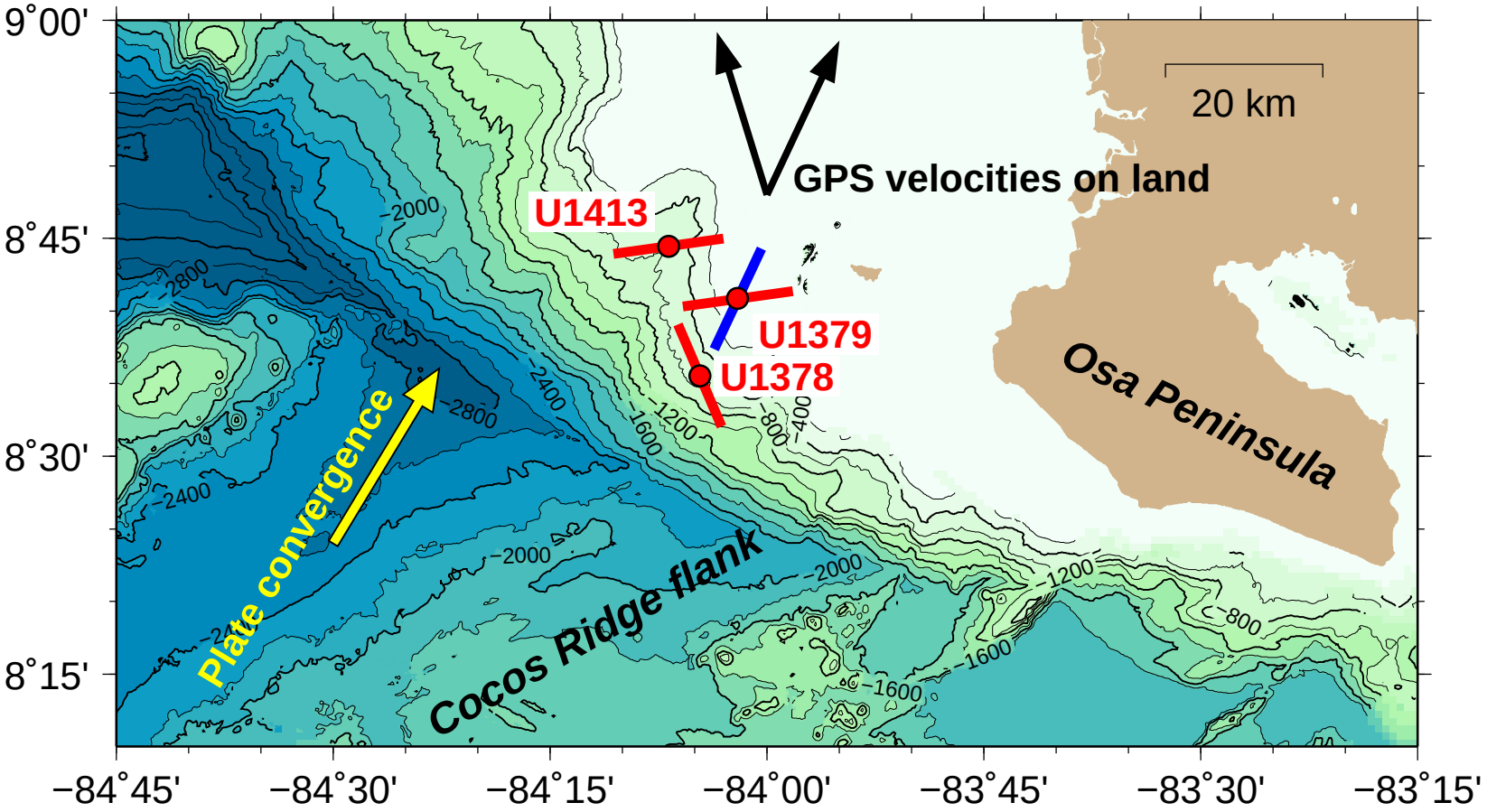
9°00'
8°45'
8°30'
8°15'
−84°45'
−84°30'
−84°15'
−84°00'
−83°45'
−83°30'
−83°15'
20 km
GPS velocities on land
U1413
U1379
U1378
Osa Peninsula
Plate convergence
Cocos Ridge flank
−2000
−2800
−2400
−1600
−1200
−800
−400